ACS APPLIED MATERIALS & INTERFACES

Research Article

www.acsami.org

Localized Order–Disorder Transitions Induced by Li Segregation in Amorphous TiO_2 Nanoparticles

Handan Yildirim,[†] Jeffrey P. Greeley,*[,†] and Subramanian K. R. S. Sankaranarayanan*[,‡]

[†]School of Chemical Engineering, Purdue University, West Lafayette, Indiana 47907, United States

[‡]Center for Nanoscale Materials, Argonne National Laboratory, 9700 S. Cass Avenue, Argonne, Illinois 60439, United States

Supporting Information

ABSTRACT: Li segregation and transport characteristics in amorphous TiO_2 nanoparticles (NPs) are studied using molecular dynamics (MD) simulations. A strong intraparticle segregation of Li is observed, and the degree of segregation is found to correlate with Li concentration. With increasing Li concentration, Li diffusivity and segregation are enhanced, and this behavior is tied to the structural response of the NPs with increasing lithiation. The atoms in the amorphous NPs undergo rearrangement in the regions of high Li concentration, introducing new pathways for Li transport and segregation. These localized atomic rearrangements, in turn, induce preferential crystallization near the surfaces of the NPs. Such rich, dynamical responses are not expected for crystalline NPs, where the presence of well-defined lattice sites leads to limited segregation and transport at high Li concentrations. The preferential crystallization in the near-surface region in amorphous NPs may offer enhanced stability and fast Li transport for Li-ion battery applications, in addition to having potentially useful properties for other materials science applications.

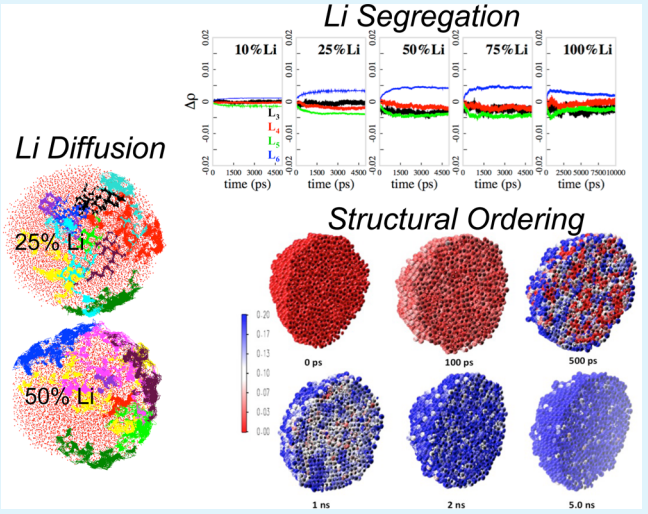

KEYWORDS: *amorphous titania, nanoparticle, lithiation, segregation, diffusion, Li-ion batteries*

INTRODUCTION

One of the greatest challenges faced by society today is the development of efficient means of storing energy. Many efforts have been made to develop efficient electrode materials with high specific energy density and excellent power performance. By means of manipulating materials chemistry, considerable advances have been made in energy storage systems based on rechargeable Li-ion batteries (LIBs).[1−3] Today, however, we have reached the performance limits of standard electrode materials, and further improvements are crucial. One of the recent efforts in this direction is to use nanomaterials and nanoscale architectures for LIB applications.[4−6] Nanoscale architectures offer unique mechanical and electrical properties resulting from confinement effects and the mixture of both bulk and surface properties. Nanoscale materials provide better accommodation of strain upon Li insertion and removal, thus improving cycle life.[7,8] They provide increased electrode/electrolyte contact area, which can yield higher charge/discharge rates. Furthermore, they also exhibit short lengths for both electronic and ionic transport. Many examples are available in the literature regarding the performance of nanostructured metal oxides, including nanotubes, nanowires, and nanoparticles (NPs) with varying morphologies such as hollow and core−shell-like structures.[9]

In LIBs, graphite-based materials have been traditionally used as anode materials. For applications in hybrid[10] and plug-in hybrid electric vehicles,[11] however, the electrode materials must offer high capacity and stability. The replacement of graphite (theoretical capacity of 372 mAh/g) with high capacity materials such as Si (4200 mAh/g) and/or Sn (980 mAh/g) has been investigated, and it has been shown that these materials experience rapid capacity degradation during cycling.[12] TiO_2, on the other hand, has a theoretical capacity of 330 mAh/g. Although the capacity is modest,[13] TiO_2 is structurally very stable, as the volume change upon Li insertion is very small (∼4%), leading to long cycle life.[14] From a safety point of view, TiO_2 has an additional advantage over the high-capacity materials. It operates at relatively high voltages (1.5−1.8 V versus Li/Li^+), thus reducing the possibility of Li dendrite formation.[15,16] At this high potential, the formation of a solid electrolyte interface (SEI) layer can also be avoided without compromising safety. Thus, TiO_2, as an anode material, has the potential to offer both safety and stability for Li-ion battery applications.

Received: July 22, 2014
Accepted: October 10, 2014
Published: October 10, 2014

In practice, the highest achievable capacity for bulk TiO_2 is only half of its theoretical value, as the Li insertion ratio above 0.5 (Li/Ti) is blocked due to strong repulsive forces between Li ions.[17] This drawback is improved by using nanoscale materials, which offer higher insertion ratios than the bulk.[13,18−23] Nanostructured TiO_2 can be found in several polymorphs, including amorphous, anatase, or rutile, depending on the details of the fabrication procedure and heat treatment.[24,25] Recent studies suggest that amorphous TiO_2 nanostructures perform better than bulk and crystalline structures, as they offer rapid Li transport and may undergo phase transitions that allow higher intercalation ratios.[26] However, understanding of the atomistic details regarding nanoscale effects on the dynamics of Li-ion transport, and the accompanying structural changes in nanostructured electrodes, has not reached the level of bulk materials, and with improved understanding, the development of nanostructured electrodes could be accelerated.

Considerable effort has been made to understand the properties of crystalline TiO_2 NPs, including their response to external pressure[27] and phase transformations,[28] as well as their photocatalytic activity.[29] The ground state properties of small TiO_2 NPs have been investigated using density functional theory (DFT),[30] and the role of surface passivation on the morphology and phase stability has been discussed.[31] Molecular dynamics (MD) simulations have been utilized to study NP sintering[32] and water interaction with TiO_2 NPs;[33] and recently, Li conductivity has also been studied in rutile NPs via multi-scale simulation methods.[34] For amorphous TiO_2 NPs, although many practical applications are available, the structural and dynamical properties, such as diffusion characteristics and compositional variation upon lithiation, are largely unexplored. For bulk amorphous systems, short-range order can lead to different features for Li intercalation and diffusion[35] compared to crystalline titania, and such differences may also exist, or even be accentuated, at the nanoscale. Obtaining insights into the atomistic origins behind these differences is important, and as mentioned above, is currently lacking.

Although only a modest amount of work on lithium/titania surface interactions has been reported in the literature, adsorption and segregation of other alkali metals on metal oxides has been previously examined in various experimental studies, with a goal of using the alkali metals to achieve controlled reduction of oxide surfaces. For example, experiments have been conducted for potassium on NiO[36] and ZnO[37] and for sodium on MgO.[38] For TiO_2, a number of experimental studies have also probed the changes in the geometry and electronic structure upon adsorption of potassium and sodium.[39−42] The adsorption of these alkali metals was shown to restructure the substrate.[42] For K adsorption on TiO_2, a K-induced band gap state is reported at about 3 eV above the valence band maximum (VBM),[40,41] indicative of a reduced surface. An analysis of K segregation to the surface of TiO_2(100), reported in an earlier experimental study,[43] showed that the concentration of K is strongly influenced by the temperature. Below 875 K, potassium was found to be at the topmost surface layer, whereas above 875 K, it was located in the subsurface layer. Finally, a recent experimental study on lithium alanate ($LiAlH_4$),[44] a promising candidate for hydrogen storage, showed the reduction of Ti^{4+} and Ti^{3+}along with the segregation of Li cations to the surface of $LiAlH_4$. These results resemble, in some respects, the Li segregation observed in TiO_2 NPs in our study, which is described in detail below.

In this contribution, we carry out a series of MD simulations to explore Li segregation and transport in amorphous TiO_2 NPs with an aim of obtaining atomistic insight into the structural response of amorphous NPs to lithiation. We report on the structural and transport characteristics of lithiated amorphous titania NPs that lead to concentration-dependent Li segregation profiles. The results indicate that there is a driving force for segregation of Li toward the surface of the NP that is strongly enhanced at high Li concentrations. On the basis of calculated changes in the configurational energies, together with the Li transport characteristics and a jump frequency analysis for Li, we conclude that the segregation leads to a rich array of nanostructural and crystallization effects that are nonuniform within the NPs. Finally, we briefly discuss the implications of our findings for LIB performance.

COMPUTATIONAL METHODS

The choice of the interaction potential for our simulation is based on the results of earlier studies,[45] which showed that the force field parameters developed by Matsui and Akaogi[46] are suitable for describing a wide range of properties of bulk TiO_2 polymorphs[47] as well as those of various nanostructures.[48] The potential is comprised of pairwise additive Coulomb dispersion and repulsive interactions. For lithiated TiO_2 NPs, we employed a recently developed polarizable force field by Kerisit et al.[49,50] in which a polarizable ion is composed of a core and shell, which share the ion's charge and are linked by a harmonic spring, k = 44.3 eV/Å^2. The core−shell interaction is described by an interaction potential defined as $U_{core-shell} = kr_{cs}^2$ where r_{cs} is the core−shell separation distance. A small mass of 0.2 au is assigned to the shells, and their motion is treated as that of the cores following the adiabatic shell model.[50] Long-range Coulomb forces and short-range interactions represent the interatomic interactions. The Buckingham potential describes the short-range interactions, and the Coulombic interactions are introduced by means of Ewald−Hansen method. The potential parameters are summarized in ref.[49] All simulations are performed using the DL POLY-MD package.[51]

We start with a stoichiometric 6 nm anatase TiO_2 NP, which corresponds to the simulation box containing 2021 TiO_2 units. The anatase NPs are generated by carving a sphere from a large bulk anatase TiO_2. To preserve the stoichiometry, the extra atoms are removed to maintain charge balance and overall neutrality. This is a standard approach applied in the literature.[52−55] Once the NP with appropriate stoichiometry is constructed by the removal of the extra atoms, we apply structural optimization (energy minimization). The simulations are performed in a cubic cell using periodic boundary conditions. To limit the interaction between the NPs and their images, a large cubic cell is used. There is a 40 Å distance between the NPs and their periodic images that is sufficient to limit artifacts from NPs interacting with their periodic images. The resulting structures are further equilibrated at 300 K for 1 ns within the canonical ensemble. Thermodynamic variables of this ensemble are temperature (T), number of particles (N), and the volume of the system (V). This constant particle, volume, and temperature ensemble is called the NVT ensemble. We then generate amorphous NPs by heating the 6 nm anatase NP to 3000 K and obtain an equilibrated melt. The melted structures are subsequently cooled at a rate of 2.5×10^{13} K/s to 350 K, and finally an amorphous TiO_2 NP is obtained at this temperature. We further simulate the unlithiated amorphous NP at this temperature for another 300 ps and then the various structural/dynamical properties are analyzed. The structural characteristics of the amorphous NPs are examined in detail using the partial radial distribution function (PRDF) of each pair (Ti−Ti, Ti−O, and O−O).

To study the lithiation behavior of the amorphous NP, the Li concentration is varied in the NPs from 10% to 100% Li (defined as Li/Ti ratio). Initially, Li ions are randomly distributed throughout the structure, and then structurally optimized (energy minimization using conjugate gradient method) before the MD simulations are performed. The purpose of the minimization procedure here is to improve the

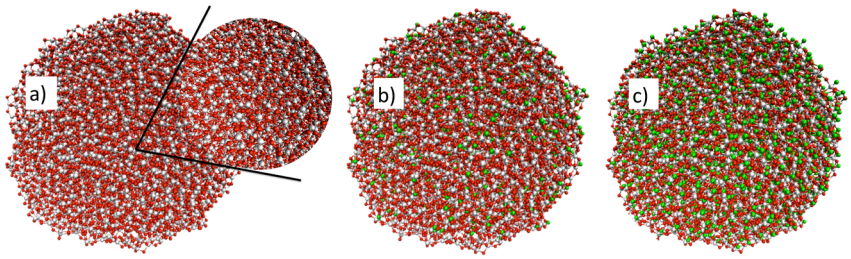

Figure 1. Optimized structures of the 6 nm amorphous TiO_2 NPs (a) unlithiated, (b) 25% lithiated, and (c) 75% lithiated. Green, red, and gray spheres represent Li, O, and Ti atoms, respectively.

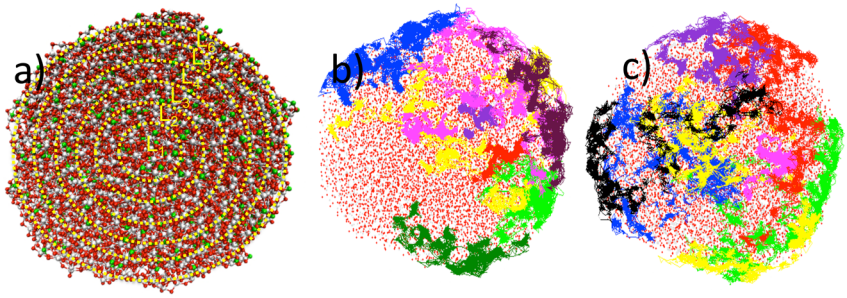

Figure 2. (a) Schematic view of the localities in the lithiated 6 nm amorphous TiO_2 NP. Each locality "L_x" is separated by 5 Å (see the discussion in the text). Trajectories of some of the segregated Li ions showing the diffusion at the surface of the amorphous TiO_2 NPs for (b) 25% Li and (c) 50% Li.

quality of the starting structure for the MD simulations. According to the DFT GGA+U description, the insertion of Li in anatase TiO_2[56] proceeds with the excess electron to be localized at the nearest Ti site, reducing Ti^{4+} to Ti^{3+} ions that give rise to a defect state in the band gap.[56,57] In our simulations, Ti^{3+} ions are incorporated as the first nearest neighbors of Li at the beginning of the simulation (0 K). A previous DFT study[56] using the GGA+U description of the lithiated TiO_2 anatase at the dilute limit showed that the position of the Ti^{3+} alters the relative energy of Li intercalation sites. The different relative Li^+-Ti^{3+} positions showed that Li interstitial sites, which are separated from the Ti^{3+}, are less favored, with the furthest considered separation leading to a 53 meV increase in energy compared to the most favored configuration. The difference between the energies of the next and the next-next nearest interstitial sites is only 4 meV, suggesting that Li-electron interaction is weak and short-ranged.

Note that the Ti^{3+} ions are not held stationary in our MD simulations and are dynamically allowed to evolve. Also, our MD simulations are performed at high temperatures, and hence the spatial distribution of Li around Ti^{3+} in the NP varies constantly. Thus, the initial distribution configuration of Ti^{3+} is quickly altered with time, and at high Li concentration, such distribution will be naturally randomized. To evaluate Li segregation and transport in an amorphous NP, MD simulations are performed within an NVT ensemble for temperatures ranging between 900 and 1400 K with 100 K intervals for 5 ns (up to 100% Li) and 10 ns for 100% Li. For the analysis of Li segregation, the NP is divided into six equally spaced regions (named as localities, from L_1 to L_6) with bin widths of 5 Å. We count the number of Li ions in each locality, and calculate the normalized density, which is defined as the number of Li ions in each locality divided by the volume, as a function of concentration and simulation time. This allows us to monitor segregation of Li and compositional fluctuation of Li ions within the NP. For evaluating Li transport, the mean square displacements (MSDs) are calculated at different temperatures, and the corresponding slopes (giving diffusion coefficients (D)) are used for constructing the Arrhenius plots. Finally, diffusion barriers (E_{diff}) and prefactors (D_0) are determined as a function of concentration from the Arrhenius plots.

RESULTS

Structures of Amorphous TiO_2 Nanoparticles. To generate amorphous TiO_2 NPs, we apply a heating and cooling procedure starting from stoichiometric anatase TiO_2 NPs. The amorphous TiO_2 NPs are chosen to be spherical based on prior experimental observations.[58] We start with several sizes of stoichiometric anatase NPs with diameters ranging from 3 to 10 nm. Amorphous NPs with diameters of approximately 6 nm are ultimately generated (details regarding the procedure for generation of amorphous NPs are discussed in the Computational Methods section). This diameter represents an intermediate size for which surface effects do not vanish completely, but at the same time, the particles are sufficiently large that these surface effects do not entirely dictate the results, as would be expected for very small NPs. The optimized structures of the 6 nm amorphous TiO_2 NP at 350 K are shown in Figure 1a, and those corresponding to 25% and 75% lithiated amorphous TiO_2 NPs are represented in Figure 1b,c. The structural characteristics of these NPs are analyzed using partial radial distribution functions (PRDF) for each atom−atom pair. The PRDFs for the amorphous NP are plotted in Figure S1a,b (Supporting Information), both at 350 and at 1400 K. The results suggest that the amorphous NP does not undergo any significant structural change at the highest temperature considered over the timescale of the simulations. Further structural analyses are made using the positions of the first peaks, the average coordination numbers, and the average bond lengths that are extracted from the PRDFs. They are summarized in Table S1 in the Supporting Information.

Li Segregation in Amorphous TiO_2 Nanoparticles. We begin with a discussion of Li diffusion and segregation in the amorphous NPs. We note that, although a well-defined diffusion mechanism can be identified for crystalline titania NPs—for instance, Li diffusion in anatase NPs proceeds via a zigzag hops between the octahedral sites[35,59−61]—a well-

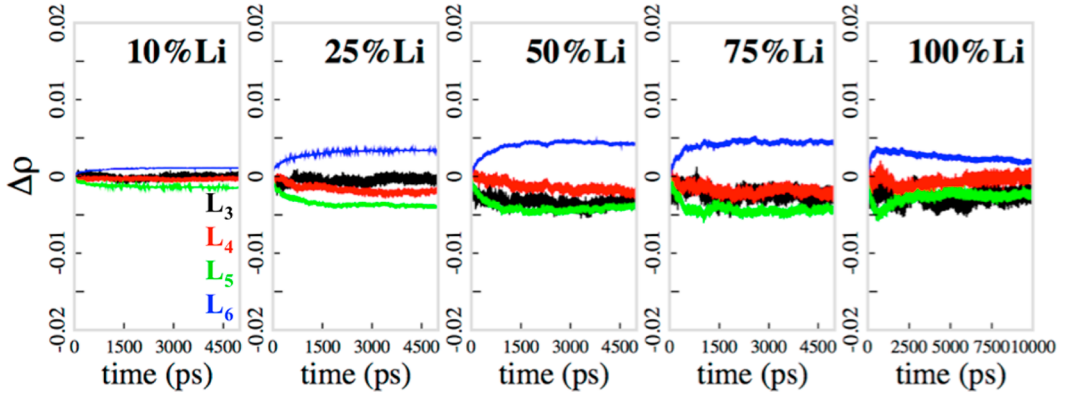

Figure 3. Change in the normalized Li density in each locality as a function of simulation time and Li concentration for 6 nm amorphous NPs. Each locality has a radial width of 5 Å, and the results are obtained from 5 ns simulations at 1200 K, with 10 ns used for the 100% Li case.

Table 1. Average Jump Frequency for Each Li Ion (jumps/s) in Amorphous NP at Varying Li Content Computed over a Simulation Time of 5 ns at 1200 K

concentration	10% Li	25% Li	50% Li	75% Li	100% Li
frequency	0.78×10^9	1.43×10^9	3.75×10^9	7.13×10^9	8.08×10^9

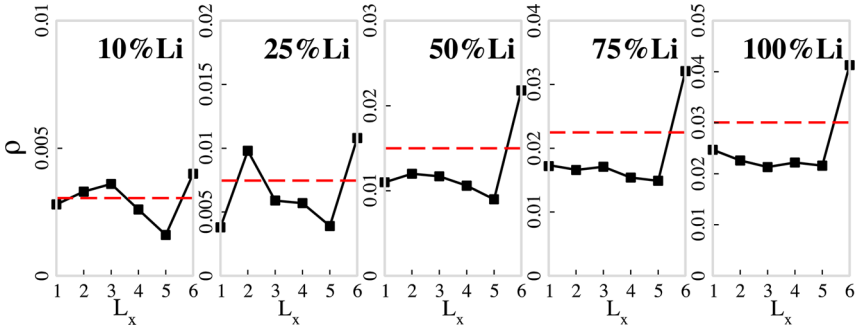

Figure 4. Normalized Li density (filled black squares) as a function of locality for each Li concentration in the equilibrated 6 nm amorphous TiO_2 NP. The dashed horizontal lines represent the homogeneous Li densities (the total number of Li atoms divided by the volume of the NP). The results are obtained from 5 ns simulations at 1200 K.

defined Li diffusion mechanism cannot be identified in amorphous TiO_2 NPs, and a more general analysis must be performed to reveal diffusion patterns. Such an analysis, described further below, suggests significant Li segregation, leading to a concentration gradient across the NP.

To reveal and quantify the degree of Li segregation, we first divide the NPs into six equally spaced regions (named "localities") with widths of 5 Å, denoted as L_1 to L_6 (see Figure 2a). The bin width, which separates the localities, is chosen to be greater than a single jump distance for Li ions between the octahedral sites in crystalline anatase NPs (such well-defined bin widths are not readily identifiable for amorphous NPs, necessitating reference to analogous crystalline systems). We then explore Li segregation in the NP for varying Li concentrations for temperature ranges between 900 and 1400 K. For simplicity, we only report the results obtained at 1200 K, but similar segregation profiles are observed at the other temperatures. We first count the number of Li in each locality as a function of time from the crossings between the localities, and then calculate the normalized Li density in each locality as a function of simulation time and Li concentration. In Figure 2b,c, we plot the trajectories of some of the segregated Li ions in the 25% and 50% lithiated 6 nm amorphous TiO_2 NPs. Each color in the figures represents the trajectory of a single Li ion extracted from the 5 ns simulation at 1200 K. Detailed analysis of the trajectories suggests that Li ions segregate toward the surface of the NPs, and with increasing Li concentration segregation is enhanced. The segregation proceeds via an initial radial movement of Li ions to the surface and then transforms into diffusion along the polar direction.

The Li segregation, which is represented by the change in the normalized Li density for the localities L_3 to L_6, obtained from the 5 ns simulations (up to 75% Li, with 10 ns used for 100% Li) at 1200 K, are summarized in Figure 3 as a function of Li concentration. The initial Li density at each locality before the relaxation of the lithiated NPs is nearly constant, with slight statistical fluctuations. The normalized Li density profile for each locality suggests that the Li density varies in these localities as the simulation time proceeds. In particular, the density fluctuations suggest a reduction in Li density in the inner localities and a corresponding increase in the outer localities for any given Li composition in the NPs. These density fluctuations suggest that there is a radially outward flow of Li towards the surface of the NPs. This leads to a net increase in Li concentration in the outer locality followed by a corresponding decrease in the inner localities. The results in turn suggest that Li segregates toward the surface of the NPs. Furthermore, we find that segregation is enhanced with increasing Li concentration in the NPs. This conclusion is

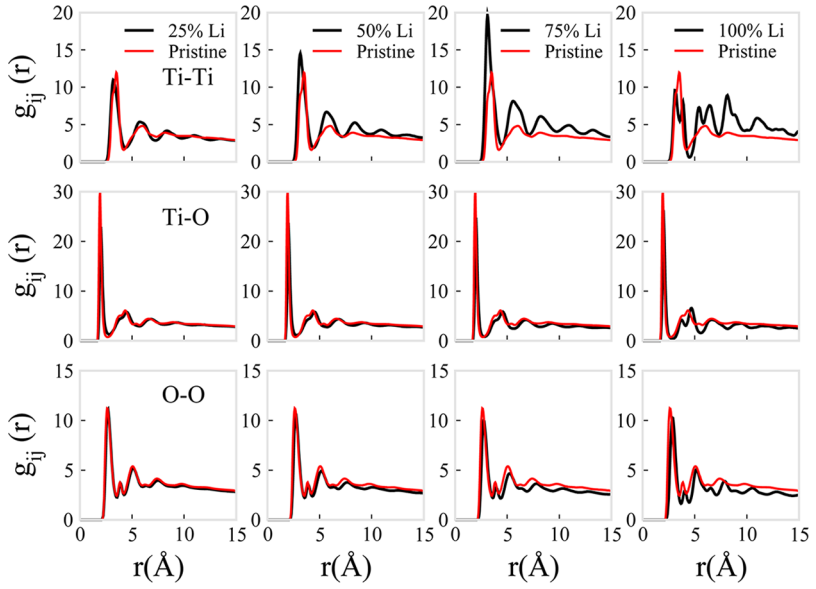

Figure 5. PRDFs for 6 nm amorphous TiO_2 NPs as a function of Li concentration obtained at 1200 K from the 5 ns simulation for Ti−Ti, Ti−O, and O−O pairs for Li concentrations of 25%, 50%, 75%, and 100% Li. The PRDFs corresponding to the pristine (unlithiated) amorphous TiO_2 NP obtained at 1200 K and 5 ns are plotted in the background of each panel for reference.

corroborated by our analysis of jump frequencies associated with Li exchange between the localities, as shown in Table 1. At the highest Li concentration, we find that initially Li segregates to the surface of the NP. The high population of Li at the surface that results from segregation ultimately increases the system energy, thus causing some of the Li at the surface to diffuse back towards the inner regions of the NP.

In Figure 4, the normalized Li densities in each locality for various Li concentrations are presented for the equilibrated (after 5 ns) amorphous NPs, along with the homogeneous initial Li densities (red dashed lines), in each locality. Our results indicate that Li segregation strongly depends on the Li segregation is a strong function of the Li concentration; a concentration-dependent enhancement is observed for the localities closest to the NPs' surface. For an average Li concentration of 10%, a reduction of 15% and 45% Li density from the localities L_4 and L_5 accompanies an increase (31%) in Li density in locality L_6. For a higher average Li concentration (50% Li), we find a reduction in the Li density from the L_3, L_4, and L_5 localities in the amount of 22%, 29%, and 40%, while an increase (46%) is obtained in the L_6 locality. We observe a similar trend for the 75% Li case. Finally, for 100% Li, the reductions of Li densities across the localities of L_2 to L_5 are 26% (L_2), 30% (L_3), 27% (L_4), and 29% (L_5), and as a result, an increase in Li density in the L_6 locality of approximately 36% is observed.

Analysis of Li Jump Frequencies in Amorphous TiO_2 Nanoparticles. Figures 3 and 4 demonstrate the existence of Li segregation in amorphous titania NPs. However, they do not directly indicate whether the segregation is thermodynamically driven (resulting from differences in Li absorption energetics between the surface and bulk of the nanoparticles) or kinetically driven (resulting from local changes in the activation barrier and hence Li diffusion coefficient), and such information is crucial to the development of a full understanding of the segregation process. To rule out the possibility of any kinetic contribution to the segregation phenomenon, we calculate the number of exchanges between the localities throughout the MD simulations. For each Li in the NPs, we count the number of forward jumps (towards the surface of the NP) from one locality to another at every 10 ps for the entire simulation time. Note that a successful jump is required to have a distance greater than the distance between octahedral sites (corresponding to the Li diffusion mechanism in crystalline anatase NPs), and the final configuration of Li must reside in a locality closer to the surface than the initial locality. With this information, the number of jumps is counted and averaged with respect to the number of Li in the NPs at each Li concentration. The averaged jump frequencies associated with each Li concentration are reported in Table 1.

The averaged Li jump frequency results suggest that Li jump frequencies gradually increase with increasing Li concentration. We observe that the frequencies (jumps/s) increase from 0.78×10^9 for 10% Li to 3.75×10^9 for 50% Li and to 8.08×10^9 for 100% Li in the amorphous TiO_2 NP. A simple back of the envelop calculation suggests that these jump frequencies are sufficiently high to make any purely kinetic contributions to the segregation phenomena unlikely. The average distance traversed by Li can be calculated as ∼ (jump frequency) × (total simulation time) × (mean distance per jump). Over a 5 ns simulation time and using a 3 Å mean jump distance, we find that the average distance that can be traversed by any Li ion is ∼3.5 nm for 50% Li concentration and ∼7.5 nm for the 100% Li case. Considering that the TiO_2 NP itself is 6 nm in diameter, the average distances traveled by Li ions imply that the ions traverse a significant fraction of the NPs within the simulation time. The results suggest that the Li ions are able to equilibrate to their thermodynamically preferred positions and that any kinetic or unsteady state contribution to the segregation phenomena are unlikely.

Li Diffusion and Structural Changes in Lithiated Amorphous TiO_2 Nanoparticles. To quantify the Li diffusion energetics for concentrations ranging from 10% to 100% Li, the averaged mean square displacements (MSDs) of Li ions are calculated for temperatures between 900 and 1400 K, and Arrhenius plots (see Figure S2, Supporting Information)

Table 2. Bond-Order Parameter (q_4 and q_6) for Face-Centered-Cubic (fcc), Hexagonal Close-Packed (hcp), Simple Cubic (sc), Body-Centered-Cubic (bcc), Icosahedral, Amorphous, and Li Titanate Crystal (100% Li) Structures[a]

							NPs		$LiTiO_2$[62]
structure	fcc	hcp	bcc	icosahe-dral	sc	amorphous	unlithiated	lithiated	
q_4	0.19094	0.09722	0.08202	0	0.76376	0	0.0−0.10	0.17−0.20	0.19010
q_6	0.57452	0.48476	0.50083	0.66332	0.35355	0	0.0−0.20	0.50−0.57	0.56493

[a]The data presented in ref 62 is for the 100% lithiated cubic structure (bulk).

are constructed from which the diffusion energetics and dynamics are determined. We find an increase in the MSDs with increasing concentration, and the highest slope corresponds to the 100% lithiated NP. In our earlier study, a concentration-dependent increase in Li transport rates was attributed to the rearrangement of the atoms in the bulk amorphous TiO_2.[35] The Arrhenius plot also suggests that Li diffusion barriers in 6 nm amorphous NPs decrease gradually with increasing Li concentration. For most concentrations, the comparison between the diffusion barriers in bulk amorphous TiO_2 and in 6 nm amorphous TiO_2 NPs shows that those of the NPs are lower, revealing a promising effect of the nanostructuring on Li transport for the majority of relevant Li concentrations. We should note, however, that the barrier associated with the 100% Li in amorphous NPs is slightly higher (55 meV) than its bulk counterpart (see Table S2, Supporting Information). We postulate this to result from a nonuniform distribution of the atomic rearrangements throughout the NP, and the diffusion parameters are determined from the averaged values over the entire system. In the 100% Li in bulk amorphous TiO_2, we observed a structural phase transition from an amorphous to a cubic phase.[62] However, as discussed above, in the amorphous TiO_2 NPs, significant Li segregation is observed, leading to a concentration gradient across the NP. The lowering in the subsurface concentration of Li in the amorphous NPs seems to lead to a delayed transition to the crystalline phase, which may explain the slight increase in the diffusion barrier. This point is further discussed below.

We also explored the atomic rearrangements of Ti and O throughout the amorphous NPs, and our analysis shows that at high Li concentrations, both Ti and O gain significant mobility, an effect that is qualitatively similar to our previous observation for the highly lithiated bulk amorphous TiO_2.[35,62] Further, the temporal analysis of the atomic density profiles suggests that Ti and O undergo an inverse motion before the equilibrium is reached (from the surface of the NP to an inner locality) that may help to facilitate the segregation of Li ions within the NPs (results not shown). This change leads to a noticeable atomic rearrangement within the lithiated amorphous NPs, thus facilitating rapid transport of Li ions.

The structural evolution of the lithiated amorphous NPs is further examined by PRDF analysis for Ti−Ti, Ti−O, and O−O pairs, and the results are plotted in Figure 5 (data for pristine (unlithiated) TiO_2 NPs are included for reference) for Li concentrations of 25%, 50%, 75%, and 100%. The PRDF results suggest a noticeable atomic rearrangement throughout the NP and show that Ti and O atoms are rearranged within the NPs with increasing Li concentration. The change in the PRDFs is particularly noticeable for Ti−Ti pairs. The flat regions, which correspond to the higher-order neighbors present in the pristine amorphous NPs, are replaced by emerging sharp peaks, which seem to become more distinct with increasing concentration. These results suggest a transition from an amorphous to an ordered structure. We also observe a slight enhancement in the ordering of Ti−O and O−O pairs. A quantitative estimate of the spatial and temporal evolution of this ordering, aided by Li-segregation, is discussed in the next section.

Li Segregation Induced Order−Disorder Transition in Amorphous TiO_2 Nanoparticles. Based on the discussions of the previous section, Li segregation appears to be driven by simple thermodynamic effects. However, it can also be affected by morphological features of the titania particles. In particular, as discussed above, the evidence from the calculated PRDFs and Li diffusion coefficients hints that Li segregation and transport induce significant changes in the extent of ordering in amorphous titania. This effect may not only have implications for battery performance but could also be a more general phenomenon in concentration-induced phase changes in nanostructures.

To provide a more detailed, molecular-level analysis of this striking effect, we compute a series of bond order parameters as a function of position and simulation time for both pristine and 100% lithiated amorphous NPs. The bond order parameter approach[63] is capable of identifying local and extended orientational symmetries in clusters and solids and of distinguishing between atoms in solid close-packed and amorphous environments. To quantify the spatial and temporal evolution of the Li-induced ordering, starting from an initial amorphous structure, we focus specifically on local bond-orientational order parameters. Spherical harmonic basis functions $Y_{lm}(\theta_{ij}, \varphi_{ij})$ are associated with every bond joining an atom to its near neighbors. Here, θ and φ refer to polar and azimuthal angles of vector $\mathbf{r}_{ij}$ in a given reference frame. The term "bond" refers to the unit vector $\mathbf{r}_{ij}$ joining a reference atom i to any neighboring atom j within a cutoff radius r_{cut}. The cutoff radius is generally taken to be 1.2 times the first minimum in the RDF. To make the bonds independent of direction, only even l-shaped harmonics are considered that are invariant under inversion. The local order around any atom i is an average over all bonds with the neighboring N_{nb} atoms, and is given by

$$q_{lm}(i) = \frac{1}{N_{nb}(i)} \sum_{j=1}^{N_{nb(i)}} Y_{lm}(r_{ij}) \tag{6}$$

A second-order invariant can be constructed to give a local order parameter independent of the choice of the reference system:

$$q_l(i) = \left(\frac{4\pi}{2l+1} \sum_{m=-l}^{l} q_{lm}(i)^2 \right)^{1/2} \tag{7}$$

The value for the local bond-order parameter, q_l, depends on the relative bond orientations, and has a unique value for each crystal structure, as shown in Table 2.

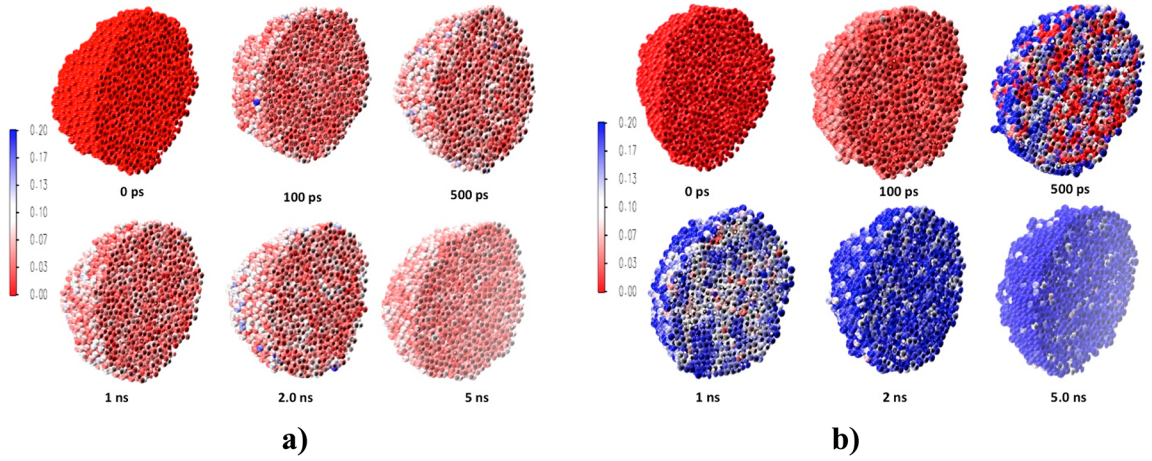

Figure 6. Spatial and temporal variation of bond orientational order parameter (q_4) for amorphous titania NPs that are (a) pristine and (b) 100% lithiated. For the sake of clarity, only the oxygen atoms are shown. The color bar indicates the magnitude of q_4.

We choose the q_4 and q_6 signatures to study the evolution of ordering in unlithiated and 100% lithiated amorphous TiO_2 NPs. Figure 6a shows the spatial variation of the q_4 signature used to evaluate the time evolution of any possible structural ordering in the unlithiated structure. For the sake of clarity, we only depict the ordering of oxygen. The spatiotemporal distribution of ordering evaluated for the unlithiated amorphous TiO_2 NP shows that the structure remains predominantly disordered, even after 5 ns. Figure 6b presents the spatiotemporal distribution of ordering for a 100% lithiated amorphous TiO_2 NP. At the start of the simulations, the structure is completely amorphous and is characterized by the q_4 values close to 0. Li then begins to segregate to the surface. The segregation of Li is associated with a corresponding change in the extent of ordering; a gradual increase in local q_4 values suggests that order is increasing in the amorphous NP. Comparison of the local q_4 values to the ideal crystal structures (see Table 2) suggests that the ordered structures resemble those of a face-centered-cubic (fcc) crystal. The ordering appears to initiate at the surface of the NP (as evidenced by higher q_4 values on the surface) where Li is segregated. It proceeds gradually to the core of the NP as a function of simulation time. At the end of the 5 ns simulation, we notice that the NP still maintains partial disorder as evidenced from the distribution of the q_4 values within the NP : light blue ($q_4 \sim$ 0.17−0.13) and white shades (~0.07−0.10). Comparison of the q_4 local bond-order parameters for the 100% lithiated and the unlithiated NPs clearly highlight the role of the Li ions and their segregation for inducing disorder−order transition in amorphous TiO_2 NPs.

The Li-induced ordering of the amorphous structures has potentially interesting implications for both energy storage applications and for more general phenomena involving phase transformations of NPs. In a previous study,[35,64] we established that the bulk cubic titania presents the lowest diffusion barrier for Li migration among various titania polymorphs and that this cubic phase can form spontaneously from amorphous titania at high Li concentrations. This behavior is also found in small NPs of amorphous titania, providing further evidence of their usefulness in Li-ion battery anode applications. If the partially crystalline shell/amorphous core morphology can be synthesized and stabilized over extended battery cycling, it might be possible to operate an electrode composed of these materials in such a manner that only the cubic shells are lithiated in a given cycle, leaving an unlithiated amorphous core that could prevent excessive strain buildup and possible distortions in NPs, resulting in enhanced battery lifetime.[65] Further, we note that this and related effects could potentially be of more general use in exploiting the properties of amorphous titanium oxide (or other oxide) NPs in materials science applications, ranging from thermoelectrics to catalysis, where a core−shell, amorphous−crystalline structure could provide enhanced stability and performance.

CONCLUSIONS

We present an atomistic simulation study investigating nanoscale effects on Li segregation and transport characteristics in amorphous TiO_2 NPs. Our results indicate that a strong driving force for Li segregation toward the surface of the NPs exists, resulting in Li enrichment near the surfaces of the amorphous NPs for essentially all Li concentrations, with more segregation tendency for high Li concentrations. The segregation is driven by thermodynamics and induces ordering near the surface of the NP due to higher Li concentrations, consistent with the results of our previous simulations on bulk amorphous titania at high Li concentrations. The crystalline outer regions of the NPs permit rapid diffusion of Li, suggesting that it may be possible to preserve an amorphous, unlithiated core in these particles, thereby limiting strain and expansion of the NPs, and making them potentially attractive as anode materials for either Li-ion batteries, as suggested by a recent experimental study,[66] or other applications where a heterogeneous oxide morphology is desirable.

ASSOCIATED CONTENT

Supporting Information

Technical details concerning the structure of the nanoparticles, the Li diffusion in the nanoparticles, and the configurations energies are presented. This material is available free of charge via the Internet at http://pubs.acs.org.

AUTHOR INFORMATION

Corresponding Authors

*J. P. Greeley. E-mail: jgreeley@purdue.edu.
*S. K. R. S. Sankaranarayanan. E-mail: skrssank@anl.gov.

Notes

The authors declare no competing financial interest.

■ ACKNOWLEDGMENTS

A DOE Early Career Award for J.G. through the U.S. Department of Energy, Office of Science, Office of Basic Energy Sciences/Chemical Sciences, is acknowledged. Use of the Center for Nanoscale Materials was supported by the U.S. Department of Energy, Office of Science, Office of Basic Energy Sciences, under Contract No: DE-AC02-06CH11357. The authors also acknowledge the use of computational resources through the National Energy Research Scientific Computing Center (NERSC). This research used resources of the National Energy Research Scientific Computing Center, a DOE Office of Science User Facility supported by the Office of Science of the U.S. Department of Energy under Contract No. DE-AC02-05CH11231.

■ REFERENCES

(1) Tarascon, J. M.; Armand, M. Issues and Challenges Facing Rechargeable Lithium Batteries. *Nature* **2001**, *414*, 359−367.
(2) Wakihara, W.; Yamamoto, O. *Lithium Ion Batteries - Fundamentals and Performance*; Kodansha-Wiley-VCH: Weinheim, Germany, 1998.
(3) Schalkwijk, V. W.; Scrosati, B. *Advances in Lithium-Ion Batteries*; Kluwer Academic/Plenum Publishers: New York, 2002.
(4) Nazar, L. F.; Goward, G.; Leroux, F.; Duncan, M.; Huang, H.; Kerr, T.; Gaubicher, J. Nanostructured Materials for Energy Storage. *Int. J. Inorg. Mater.* **2001**, *3*, 191−200.
(5) Hirscher, M. Nanoscale Materials for Energy Storage. *Mater. Sci. Eng., B* **2004**, *108*, 1.
(6) Thackeray, M. M. Manganese Oxides for Lithium Batteries. *Prog. Solid State Chem.* **1997**, *25*, 1−71.
(7) Graetz, J.; Ahn, C. C.; Yazami, R.; Fultz, B. Highly Reversible Lithium Storage in Nanostructured Silicon. *Electrochem. Solid-State Lett.* **2003**, *6*, A194−A197.
(8) Talyosef, Y.; Markovsky, B.; Lavi, R.; Salitra, G.; Aurbach, D.; Kovacheva, D.; Gorova, M.; Zhecheva, E.; Stoyanova, R. Comparing the Behavior of Nano- and Microsized Particles of $LiMn_{1.5}Ni_{0.5}O_4$ Spinel as Cathode Materials for Li-Ion Batteries. *J. Electrochem. Soc.* **2007**, *154*, A682−A691.
(9) Ren, Y.; Liu, Z.; Pourpoint, F.; Armstrong, A. R.; Grey, C. P.; Bruce, P. C. Nanoparticulate TiO_2(B): An Anode for Lithium-Ion Batteries. *Angew. Chem., Int. Ed.* **2012**, *51*, 2164−2167.
(10) Amine, K.; Belharouak, I.; Chen, Z.; Tran, T.; Yumoto, H.; Ota, N.; Myung, S.-T.; Sun, Y.-K. Nanostructured Anode Material for High-Power Battery System in Electric Vehicles. *Adv. Mater.* **2010**, *22*, 3052−3057.
(11) Zhou, H.; Wang, Y.; Li, H.; He, P. The Development of a New Type of Rechargeable Batteries Based on Hybrid Electrolytes. *ChemSusChem* **2010**, *3*, 1009−1019.
(12) Park, C.-M.; Kim, J.-H.; Kim, H.; Sohn, H.-J. Li-Alloy based Anode Materials for Li Secondary Batteries. *Chem. Soc. Rev.* **2010**, *39*, 3115−3141.
(13) Yang, Z.; Choi, D.; Kerisit, S.; Rosso, K. M.; Wang, D.; Zhang, J.; Graff, G.; Liu, J. J. Nanostructures and Lithium Electrochemical Reactivity of Lithium Titanites and Titanium Oxides: A Review. *Power Sources* **2009**, *192*, 588−598.
(14) Wagemaker, M.; Kearley, G. J.; Van Well, A. A.; Mutka, H.; Mulder, F. M. Multiple Li Positions Inside Oxygen Octahedra in Lithiated TiO_2 Anatase. *J. Am. Chem. Soc.* **2003**, *125*, 840−848.
(15) Liu, X. H.; Zhong, Li.; Zhang, Q. L.; Kushima, A.; Mao, S. X.; Li, J.; Ye, Z. Z.; Sullivan, J. P.; Huang, J. Y. Lithium Fiber Growth on the Anode in a Nanowire Lithium Ion Battery During Charging. *Appl. Phys. Lett.* **2011**, *98*, 183107.
(16) Bhattacharyya, R.; Key, B.; Chen, H. L.; Best, A. S.; Hollenkamp, A. F.; Grey, C. P. In Situ NMR Observation of the Formation of Metallic Lithium Microstructures in Lithium Batteries. *Nat. Mater.* **2010**, *9*, 504−510.
(17) Nuspl, G.; Yoshizawa, K.; Yamabe, T. Lithium Intercalation in TiO_2 Modifications. *J. Mater. Chem.* **1997**, *7*, 2529−2536.
(18) Kavan, L.; Rathouský, J.; Grätzel, M.; Shklover, V.; Zukal, A. Surfactant-Templated TiO_2 (Anatase): Characteristic Features of Lithium Insertion Electrochemistry in Organized Nanostructures. *J. Phys. Chem. B* **2000**, *104*, 12012−12020.
(19) Tang, Y.; Yang, L.; Qiu, Z.; Huang, J. Template-Free Synthesis of Mesoporous Spinel Lithium Titanate Microspheres and Their Application in High-Rate Lithium Ion Batteries. *J. Mater. Chem.* **2009**, *19*, 5980−5984.
(20) Sudant, G.; Baudrin, E.; Larcher, D.; Tarascon, J.-M. Electrochemical Lithium Reactivity with Nanotextured Anatase-Type TiO_2. *J. Mater. Chem.* **2005**, *15*, 1263−1269.
(21) Jiang, C.; Wei, M.; Qi, Z.; Kudo, T.; Honma, I.; Zhou, H. Particle Size Dependence of the Lithium Storage Capability and High Rate Performance of Nanocrystalline Anatase TiO_2 Electrode. *J. Power Sources* **2007**, *166*, 239−243.
(22) Fattakhova-Rohlfing, D.; Wark, M.; Brezesinski, T.; Smarsly, B. M.; Rathouský, J. Highly Organized Mesoporous TiO_2 Films with Controlled Crystallinity: A Li-Insertion Study. *Adv. Funct. Mater.* **2007**, *17*, 123−132.
(23) Kubiak, P.; Geserick, J.; Hüsing, N.; Wohlfahrt-Mehrens, M. Electrochemical Performance of Mesoporous TiO_2 Anatase. *J. Power Sources* **2008**, *175*, 510−516.
(24) Swamy, V.; Kuznetsov, A.; Dubrovinsky, L. S.; McMillan, P. F.; Prakapenka, V. B.; Shen, G.; Muddle, B. C. Size-Dependent Pressure-Induced Amorphization in Nanoscale TiO_2. *Phys. Rev. Lett.* **2006**, *96*, 135702.
(25) Gratzel, M. Photoelectrochemical Cells. *Nature* **2001**, *414*, 338−344.
(26) Liu, H.; Bi, Z.; Sun, X.-G.; Unocic, R. R.; Paranthaman, M. P.; Dai, S.; Brown, G. M. Mesoporous TiO_2−B Microspheres with Superior Rate Performance for Lithium Ion Batteries. *Adv. Mater.* **2011**, *23*, 3450−3454.
(27) Swamy, V.; Kuznetsov, A.; Dubrovinsky, L. S.; Kurnosov, A.; Prakapenka, V. B. Unusual Compression Behavior of Anatase TiO_2 Nanocrystals. *Phys. Rev. Lett.* **2009**, *103*, 075505.
(28) Bassi, A. L.; Cattaneo, D.; Russo, V.; Bottani, C. E.; Barborini, E.; Mazza, T.; Piseri, P.; Milani, P.; Ernst, F. O.; Wegner, K.; Pratsinis, S. E. Raman Spectroscopy Characterization of Titania Nanoparticles Produced by Flame Pyrolysis: The Influence of Size and Stoichiometry. *J. Appl. Phys.* **2005**, *98*, 074305.
(29) Thompson, T. L.; Yates, J. T. Surface Science Studies of the Photoactivation of TiO_2 New Photochemical Processes. *Chem. Rev.* **2006**, *106*, 4428−4453.
(30) Woodley, S. M.; Hamad, S.; Mejias, J. A.; Catlow, C. R. A. Properties of Small TiO_2, ZrO_2 and HfO_2 Nanoparticles. *J. Mater. Chem.* **2006**, *16*, 1927−1933.
(31) Barnard, A. S.; Zapol, P. Effects of Particle Morphology and Surface Hydrogenation on the Phase Stability of TiO_2. *Phys. Rev. B* **2004**, *70*, 235403.
(32) Koparde, V. N.; Cummings, P. T. Molecular Dynamics Simulation of Titanium Dioxide Nanoparticle Sintering. *J. Phys. Chem. B* **2005**, *109*, 24280−24287.
(33) Hammer, B.; Wendt, S.; Besenbacher, F. Water Adsorption on TiO_2. *Top. Catal.* **2010**, *53*, 423−430.
(34) Yu, J.; Sushko, M. L.; Kerisit, S.; Rosso, K. M.; Liu, J. Kinetic Monte Carlo Study of Ambipolar Lithium Ion and Electron−Polaron Diffusion into Nanostructured TiO_2. *J. Phys. Chem. Lett.* **2012**, *3*, 2076−2081.
(35) Yildirim, H.; Greeley, J.; Sankaranarayanan, S. K. R. S. Effect of Concentration on the Energetics and Dynamics of Li Ion Transport in Anatase and Amorphous TiO_2. *J. Phys. Chem. C* **2011**, *115*, 15661−156673.
(36) Kennou, K.; Kamaratos, M.; Papageorgopoulos, C. A. Potassium Adsorption on NiO(100). *Vacuum* **1990**, *41*, 22−24.
(37) Purdie, D.; Muryn, C. A.; Crook, S.; Wincott, P. L.; Thornton, G.; Fischer, D. A. Potassium Bond Site in $ZnO(000\bar{1})p(2 \times 2)K$. *Surf. Sci. Lett.* **1993**, *290*, L680−L684.

(38) Onishi, H.; Egawa, C.; Aruga, T.; Iwasawa, Y. Adsorption of Na Atoms and Oxygen-Containing Molecules on MgO(100) and (111) Surfaces. *Surf. Sci.* **1987**, *191*, 479−491.
(39) Casanova, R.; Prabhakaran, K.; Thornton, G. Potassium Adsorption on TiO_2(100). *J. Phys.: Condens. Matter* **1991**, *3*, S91.
(40) Hardman, P. J.; Casanova, R.; Prabhakaran, K.; Muryn, C. A.; Wincott, P. L.; Thornton, G. Electronic Structure Effects of Potassium Adsorption on TiO_2(100). *Surf. Sci.* **1991**, *269/270*, 677−681.
(41) Prabhakaran, V.; Purdie, D.; Casanova, R.; Muryn, C. A.; Hardman, P. J.; Wincott, P. L.; Thornton, G. Alkali-Metal-to-Substrate Charge Transfer in TiO_2(100)$c(2 \times 2)$K. *Phys. Rev. B* **1992**, *45*, 6969.
(42) Murray, P. W.; Condon, N. G.; Thornton, G. Na Adsorption Sites on TiO_2(110)−1 × 2 and Its 2 × 2 Superlattice. *Surf. Sci.* **1994**, *323*, L281−L286.
(43) Herman, G. S.; Peden, C. H. F. Segregation of K at the TiO_2(100) Surface. *Colloids Surf., A* **1999**, *154*, 187−192.
(44) Amama, P. B.; Grant, J. T.; Shamberger, P. J.; Voevodin, A. A.; Fisher, T. S. Improved Dehydrogenation Properties of Ti-Doped $LiAlH_4$: Role of Ti Precursors. *J. Phys. Chem. C* **2012**, *116*, 21886−21894.
(45) Collins, D. R.; Smith, W. *Council for the Central Laboratory of Research Councils*; Research Report DL-TR-96-001; Daresbury Laboratory: Warrington, U. K., 1996.
(46) Matsui, M.; Akaogi, M. Molecular Dynamics Simulation of the Structural and Physical Properties of the Four Polymorphs of TiO_2. *Mol. Simul.* **1991**, *6*, 239−244.
(47) Collins, D. R.; Smith, W.; Harrison, N. M.; Forester, T. R. Molecular Dynamics Study of TiO_2 Microclusters. *J. Mater. Chem.* **1996**, *6*, 1385−1390.
(48) Bandura, A. V.; Kubicki, J. D. Derivation of Force Field Parameters for TiO_2−H_2O Systems from Ab Initio Calculations. *J. Phys. Chem. B* **2003**, *107*, 11072−11081.
(49) Kerisit, S.; Rosso, K. M.; Yang, Z.; Liu, J. Dynamics of Coupled Lithium/Electron Diffusion in TiO_2 Polymorphs. *J. Phys. Chem. C* **2009**, *113*, 20998−21007.
(50) Kerisit, S.; Deskins, N. A.; Rosso, K. M.; Dupuis, M. A Shell Model for Atomistic Simulation of Charge Transfer in Titania. *J. Phys. Chem. C* **2008**, *112*, 7678−7688.
(51) Smith, W.; Todorov, I. T. A Short Description of DL POLY. *Mol. Simul.* **2006**, *32*, 935−943.
(52) Naicker, P. K.; Cummings, P. T.; Zhang, H.; Banfield, J. F. Characterization of Titanium Dioxide Nanoparticles Using Molecular Dynamics Simulations. *J. Phys. Chem. B* **2005**, *109*, 15243−15249.
(53) Kaur, K.; Prakash, S.; Goyal, N.; Singh, R.; Entel, P. Structure Factor of Amorphous TiO_2 Nanoparticle: Molecular Dynamics Study. *J. Non-Cryst. Solids* **2011**, *357*, 3399−3404.
(54) Koparde, V. N.; Cummings, P. T. Sintering of Titanium Dioxide Nanoparticles: A Comparison Between Molecular Dynamics and Phenomenological Modeling. *J. Nanopart. Res.* **2008**, *10*, 1169−1182.
(55) Koparde, V. N.; Cummings, P. T. Molecular Dynamics Study of Water Adsorption on TiO_2 Nanoparticles. *J. Phys. Chem. C* **2007**, *111*, 6920−6926.
(56) Morgan, B. J.; Watson, G. W. GGA+*U* Description of Lithium Intercalation into Anatase TiO_2. *Phys. Rev. B* **2010**, *82*, 144119.
(57) Sodergren, S.; Siegbahn, H.; Rensmo, H.; Lindstrom, H.; Hagfeldt, A.; Lindquist, S.-E. Microscopic Solvation Process of Alkali Atoms in Finite Clusters: Photoelectron and Photoionization Studies of $M(NH_3)_n$ and $M(H_2O)_n$ (M = Li, Li, Na). *J. Phys. Chem. B* **1997**, *101*, 3078−3087.
(58) Xia, B.; Li, W.; Zhang, B.; Xie, Y. Low Temperature Vapor-Phase Preparation of TiO_2 Nanopowders. *J. Mater. Sci.* **1999**, *34*, 3505−3511.
(59) Olson, C. L.; Nelson, J.; Islam, M. S. Defect Chemistry, Surface Structures, and Lithium Insertion in Anatase TiO_2. *J. Phys. Chem. B* **2006**, *110*, 9995−10001.
(60) Koudriachova, M. V.; Harrison, N. M.; de Leeuw, S. W. Effect of Diffusion on Lithium Intercalation in Titanium Dioxide. *Phys. Rev. Lett.* **2001**, *86*, 1275.
(61) Yildirim, H.; Greeley, J. P.; Sankaranarayanan, S. K. R. S. The Effect of Concentration on Li Diffusivity and Conductivity in Rutile TiO_2. *Phys. Chem. Chem. Phys.* **2012**, *14*, 4565−4576.
(62) Yildirim, H.; Greeley, J.; Sankaranarayanan, S. K. R. S. Concentration-Dependent Ordering of Lithiated Amorphous TiO_2. *J. Phys. Chem. C* **2013**, *117*, 3834−3845.
(63) Steinhardt, P. J.; Nelson, D. R.; Ronchetti, M. Bond-Orientational Order in Liquids and Glasses. *Phys. Rev. B* **1983**, *28*, 784.
(64) Xiong, H.; Yildirim, H.; Shevchenko, E. V.; Prakapenka, V. B.; Koo, B.; Slater, M. D.; Balasubramanian, M.; Sankaranarayanan, S. K. R. S.; Greeley, J. P.; Tepavcevic, S.; Dimitrijevic, N. M.; Podsiadlo, P.; Johnson, C. S.; Rajh, T. Self-Improving Anode for Lithium-Ion Batteries Based on Amorphous to Cubic Phase Transition in TiO2 Nanotubes. *J. Phys. Chem. C* **2012**, *116*, 3181−3187.
(65) Xiong, H.; Yildrim, H.; Podsiadlo, P.; Zhang, J.; Prakapenka, V. B.; Greeley, J. P.; Shevchenko, E. V.; Zhuravlev, K. K.; Tkachev, S.; Sankaranarayanan, S. K. R. S.; Rajh, T. Compositional Tuning of Structural Stability of Lithiated Cubic Titania via Vacancy Filling Mechanism under High Pressure. *Phys. Rev. Lett.* **2013**, *110*, 078304.
(66) Borghols, W. J. H.; Lützenkirchen-Hecht, D.; Haake, U.; Chan, W.; Lafont, U.; Kelder, E. M.; van Eck, E. R. H.; Kentgens, A. P. M.; Mulder, F. M.; Wagemaker, M. Lithium Storage in Amorphous TiO_2 Nanoparticles. *J. Electrochem. Soc.* **2010**, *157*, A582−A588.